This is a preprint, the final version is subject to change, of the American Mineralogist (MSA)
Cite as Authors (Year) Title. American Mineralogist, in press.
(DOI will not work until issue is live.) DOI: http://dx.doi.org/10.2138/am-2015-4818

Revision 2

High-pressure high-temperature transitions in $MgCr_2O_4$ and crystal structures of new $Mg_2Cr_2O_5$ and post-spinel $MgCr_2O_4$ phases with implications for ultra-high pressure chromitites in ophiolites

Takayuki Ishii[1], Hiroshi Kojitani[1], Kiyoshi Fujino[2], Hitoshi Yusa[3], Daisuke Mori[1], Yoshiyuki Inaguma[1], Yoshitaka Matsushita[3], Kazunari Yamaura[3] and Masaki Akaogi[1]

[1]Department of Chemistry, Gakushuin University, Mejiro, Toshima-ku, Tokyo 171-8588, Japan

[2]Geodynamics Research Center, Ehime University, Matsuyama, Ehime 790-8577, Japan

[3]National Institute of Materials Science, Namiki, Tsukuba 305-0044, Japan

Abstract

We determined phase relations in $MgCr_2O_4$ at 12-28 GPa and 1000-1600°C using a multianvil apparatus. At 12-15 GPa, spinel-type $MgCr_2O_4$ (magnesiochromite) first decomposes into a mixture of new $Mg_2Cr_2O_5$ phase + corundum-type Cr_2O_3 at 1100-1600 °C, but it dissociates first into MgO periclase + corundum-type Cr_2O_3 at 1000°C. At about 17-19 GPa, the mixture of $Mg_2Cr_2O_5$ phase + corundum-type Cr_2O_3 transforms to a single $MgCr_2O_4$ phase. Structure refinements using synchrotron X-ray powder diffraction data indicated that the high-pressure $MgCr_2O_4$ phase has a $CaTi_2O_4$-type structure (*Cmcm*), and that the basic structure of the $Mg_2Cr_2O_5$ phase is the same as that of recently found modified ludwigite-type $Mg_2Al_2O_5$ and

$Fe_2Cr_2O_5$ (*Pbam*). The phase relations in this study may suggest that natural chromitites in the Luobusa ophiolite regarded as the deep-mantle origin were derived from the mantle shallower than the depths corresponding to pressure of 12-15 GPa because of absence of the assemblage of $(Mg,Fe)_2Cr_2O_5 + Cr_2O_3$ in the chromitites.

Keywords: Post-spinel, Rietveld refinement, crystal structure, high pressure, phase transition, magnesiochromite, calcium titanate, chromitite, ophiolite

Introduction

Chromium-bearing spinel is widely found in igneous and metamorphic rocks as an accessory mineral, and is accepted as an important indicator for petrogenesis (e.g. Sack and Ghiorso, 1991). $MgCr_2O_4$ spinel (magnesiochromite) is a major endmember of chromian spinel in mantle-derived peridotites. It is also the commercially available ore mineral of chromium. At ambient conditions, $MgCr_2O_4$ spinel has the normal spinel structure (space group *Fd-3m*) in which Mg^{2+} and Cr^{3+} occupy the tetrahedral and octahedral sites, respectively (O'Neill and Dollase, 1994).

High-pressure transition of $A^{2+}B^{3+}{}_2O_4$ spinel (post-spinel transition) has been extensively studied in various compounds to clarify host phases of trivalent cations such as Al^{3+}, Cr^{3+} and Fe^{3+} in the deep mantle. The $CaFe_2O_4$(CF)- and $CaTi_2O_4$(CT)-structured phases of $A^{2+}B^{3+}{}_2O_4$ are major post-spinel phases. Both the $CaFe_2O_4$-type structure (*Pnma*) and $CaTi_2O_4$-type structure (*Cmcm*) consist of double chains of edge-shared $B^{3+}O_6$ octahedra running parallel to one of orthorhombic cell axes, in which A^{2+} ions occupy tunnel spaces surrounded by corner-sharing of four double chains, though the $CaFe_2O_4$- and $CaTi_2O_4$-type structures have

different frameworks of $B^{3+}O_6$ octahedra. Yong et al. (2012) showed very recently that a cubic-to-tetragonal transition occurred in $MgCr_2O_4$ spinel at about 20 GPa and room temperature, based on X-ray diffraction and Raman spectroscopy at high pressure. However, high-pressure and high-temperature behaviors of $MgCr_2O_4$ spinel are not still clarified.

We recently found that $MgAl_2O_4$ spinel first decomposes into $Mg_2Al_2O_5$ + Al_2O_3 at about 20 GPa above 2000 °C and $FeCr_2O_4$ chromite into $Fe_2Cr_2O_5$ + Cr_2O_3 at about 14 GPa and 1200 °C, prior to transitions to CF- or CT-phase at higher pressure (Enomoto et al., 2009, Kojitani et al., 2010, Ishii et al., in press). The $Mg_2Al_2O_5$ and $Fe_2Cr_2O_5$ phases have the same structure named modified ludwigite (mLd) structure (*Pbam*) in which edge- and corner-shared $(Mg,Al)O_6$ or $(Fe,Cr)O_6$ octahedra are running parallel to c-axis and tunnel spaces surrounded by the octahedral chains are occupied by six-coordinated Mg^{2+} or Fe^{2+} (Enomoto et al., 2009; Ishii et al., in press).

In chromitites composed of $MgCr_2O_4$-rich, $FeCr_2O_4$-bearing spinel in the Luobusa ophiolite, Tibet, high-pressure minerals such as diamond and coesite were recently discovered (Yang et al., 2007; Yamamoto et al., 2009; Dobrzhinetskaya et al., 2009). Based on the natural observations, the deep-mantle origin of the chromitites has been discussed (Yang et al., 2007; Arai, 2010, 2013; Yamamoto et al., 2009). Ishii et al. (in press) suggested a possible depth limit for origin of the chromitites of the Luobusa ophiolite, based on phase relations in $FeCr_2O_4$ at high pressure and high temperature. However, it would be desirable to discuss the issue using the high-pressure high-temperature phase relations of both $MgCr_2O_4$ and $FeCr_2O_4$.

In this study, we have investigated in detail the phase relations of $MgCr_2O_4$ up to 28 GPa and 1600 °C, and have found dissociation of $MgCr_2O_4$ spinel into $Mg_2Cr_2O_5$ + Cr_2O_3 and subsequent recombination to the

post-spinel $MgCr_2O_4$ phase with increasing pressure. We have analyzed structures of the $Mg_2Cr_2O_5$ and $MgCr_2O_4$ phases, resulting in that the two phases have the modified ludwigite (mLd)-type and $CaTi_2O_4$ (CT)-type structures, respectively. The outline of our results on the structural and phase transition studies was presented in Ishii et al. (2013). In this study, we have also compared our results on structure analysis of CT-type $MgCr_2O_4$ with those of Bindi et al. (2014) who very recently studied the structure of CT-type $MgCr_2O_4$. Finally, based on our studies on the high-pressure phase relations and the crystal structures, we discuss on the origin of chromitites in the Luobusa ophiolite.

Experimental methods

1. High-pressure high-temperature experiments

$MgCr_2O_4$ spinel was prepared from a stoichiometric mixture of reagent grade MgO and Cr_2O_3. The mixture was heated at 1300°C for 12 h in CO_2 gas flow, and the recovered sample was finely ground and heated again at the same conditions. After twice heating for 24 h in total, it was confirmed that the product was single-phase spinel with $MgCr_2O_4$ composition by a powder X-ray diffractometer and a scanning electron microscope with an energy dispersive X-ray spectrometer (SEM-EDS). The lattice parameter of $MgCr_2O_4$ spinel, a = 8.3344(2) Å, measured by the powder X-ray diffraction did not change by the twice-heating processes, and is consistent with that by O'Neill and Dollase (1994) within the errors. The $MgCr_2O_4$ spinel thus prepared was used as the starting material for high-pressure experiments in $MgCr_2O_4$. A mixture of the synthesized $MgCr_2O_4$ spinel and MgO with a 1:1 molar ratio was used as the starting material for synthesis of $Mg_2Cr_2O_5$ phase.

The high-pressure high-temperature experiments were made at 12-28 GPa and 1000-1600°C with a Kawai-type 6-8 multianvil high-pressure apparatus at Gakushuin University. Tungsten carbide anvils with truncated edge lengths of 2.5 and 5.0 mm were used with pressure media of 5 wt% Cr_2O_3-doped MgO octahedra of 7 and 10 mm edge-lengths, respectively. A cylindrical rhenium furnace was placed in the central part of the magnesia octahedron. A $LaCrO_3$ sleeve was put outside of the rhenium heater and $LaCrO_3$ end-plugs at both ends of the heater for thermal insulation. Temperature was measured at the central part of outer surface of the furnace with a Pt/Pt-13%Rh thermocouple of 0.1 mm in diameter, without any correction for pressure effect on electromotive force of the thermocouple. Uncertainty of temperature in the present quench experiments was estimated to be about ±20°C. Phase relations of $MgCr_2O_4$ were examined using the multi-sample cell technique described in Ishii et al. (2011, 2012). The starting material of $MgCr_2O_4$ and one of pressure markers (Mg_2SiO_4, $MgSiO_3$ and $MgO+Al_2O_3$) were packed in two holes of 0.2 mm diameter in a Re capsule which was 1.0 mm in diameter and 0.7 mm in thickness. The two Re discs of 1.0 mm in diameter and 0.025 mm in thickness were placed at both sides of the Re capsule. A boron nitride capsule containing the Re capsule + discs was inserted into the central part of the tubular rhenium heater. The syntheses of $MgCr_2O_4$ and $Mg_2Cr_2O_5$ high-pressure phases used for the structure refinements were made with Pt capsules of 1.6 and 2.2 mm in diameter, respectively. A BN sleeve was placed between the Pt capsule and the Re heater for electrical insulation.

Pressure was calibrated in a similar manner to those of Ishii et al. (2011, 2012). Pressure calibration at room temperature was made using semiconductor-metal transitions of ZnS (15.5 GPa), GaAs (18.3 GPa) and GaP (23 GPa) (Dunn and Bundy, 1978, Ito, 2007). The effect of temperature on pressure was corrected at

1600°C by using Mg_2SiO_4 forsterite-wadsleyite transition (15.1 GPa) (Morishima et al., 1994), Mg_2SiO_4 wadsleyite-ringwoodite transition (21.3 GPa) (Suzuki et al., 2000), $MgSiO_3$ akimotoite-perovskite transition (22.3 GPa) (Fei et al., 2004), and transition of Al_2O_3 corundum + MgO periclase to $MgAl_2O_4$ calcium ferrite (24.9 GPa) (Irifune et al., 2002), using the pressure markers ($MgSiO_3$, Mg_2SiO_4 and MgO + Al_2O_3) packed in one of the two holes of the Re capsule. Relative uncertainty of pressure was estimated to be about ±0.2 GPa (Ishii et al., 2011, 2012).

In each run, pressure was raised to a targeted pressure of 11-28 GPa at almost constant rate during 2-4 h, and then temperature was raised to 1000-1600°C at a rate of about 100°C/min. The sample assembly was kept for 1-2 h at the desired pressure-temperature conditions. Then it was quenched to room temperature under pressure, and pressure was released slowly to ambient pressure. The recovered Re capsule holding the samples was mounted on a slide glass plate with epoxy resin, and was polished into flat to expose the samples for phase identification and composition analysis.

The phase identifications of the recovered samples were made using a microfocus X-ray diffractometer (Rigaku RINT 2500V, MDG) with an X-ray beam collimated to 50 μm in diameter. To determine lattice parameters of samples synthesized for structure refinements, powder X-ray diffraction measurements were performed with the step-scan mode (step size of 0.02°) in the 2θ range of 10-140° using the powder X-ray diffractometer (Rigaku RINT 2500V). The cell parameters determined in this way were used as initial values for Rietveld refinements, as shown below. Both the X-ray diffraction measurements were conducted using monochromatized CrKα radiation at 45 kV and 250 mA. The scanning electron microscope (SEM, JEOL JMS-6360) operated with acceleration voltage of 15 kV and probe current of 0.43 nA combined with the energy

dispersive X-ray spectrometer (EDS, Oxford INCA energy 300) was used to analyze compositions and to identify phases in the recovered samples. The natural enstatite and synthetic Cr_2O_3 eskolaite were used as standard materials for Mg and Cr, respectively. The analyzed compositions of 5-15 analysis points of each sample were averaged, and were shown with the standard deviation.

2. Synchrotron X-ray diffraction measurements and Rietveld structure refinements

For structural analyses of CT-type $MgCr_2O_4$ and the $Mg_2Cr_2O_5$ phase, angle-dispersive synchrotron powder X-ray diffraction data were obtained in the BL15XU (NIMS beam line) and BL02B2 at SPring-8. To collect the diffraction data of the samples at ambient conditions, we used an imaging plate as the detector and a Debye-Scherrer camera in a 2θ angle from 0-60° and 0-75° with an angle resolution of 0.003° and 0.01° in BL15XU and BL02B2, respectively. The incident X-ray beam in BL15XU was monochromatized at K absorption edge of niobium (λ = 0.65297 Å). The wavelength of X-ray in BL02B2 was determined from the data measured for fluorite-type CeO_2 (λ = 0.41927 Å). The synthesized polycrystalline samples were finely ground using an agate mortar, and each of them was put into a Lindemann glass capillary. During the diffraction pattern measurement, the sample was rotated to reduce the preferred orientation effect.

Rietveld analysis was made using the RIETAN-FP/VENUS package (Izumi and Momma, 2007). The initial structure models of CT-type $MgCr_2O_4$ and $Mg_2Cr_2O_5$ phase were $CaTi_2O_4$ (Bertaut and Blum, 1956) and $Mg_2Al_2O_5$ (Enomoto et al., 2009), respectively. The initial values of cell parameters in the Rietveld analysis of each sample were determined from the powder X-ray diffraction patterns (CrKα) using DICVOL06 software (Loüer and Boultif, 2007). A small amount of corundum-type Cr_2O_3 was included as the second phase in the

Rietveld analysis of CT-type $MgCr_2O_4$. In the initial stage of the Rietveld analyses for both the phases, we used the X-ray diffraction data collected in BL02B2, and subsequently used the data of BL15XU. Although both of the data sets lead to the same structure for each phase, the results using the data of BL15XU were of higher quality as the structure refinements and are shown in the following.

Results and discussion

1. High-pressure phase transitions in $MgCr_2O_4$.

Table 1 summarizes results of the phase transition experiments in $MgCr_2O_4$. Some typical microfocus X-ray diffraction patterns at room P-T conditions of the starting material and recovered samples are shown in Figure 1. The XRD pattern of starting material shows the only peaks of $MgCr_2O_4$ magnesiochromite and those of recovered samples are different from that of the starting material, excepting for that of Run no. 20. Figure 2 illustrates the phase relations in $MgCr_2O_4$ up to 28 GPa and 1600°C. Table 2 indicates analyzed chemical compositions by the SEM-EDS for new high-pressure phases in the run products with that of the starting material. At 1100-1600°C, $MgCr_2O_4$ spinel first decomposes into a mixture of a new phase and corundum-type Cr_2O_3 (eskolaite) in the pressure range of 12-15 GPa. This phase change is shown in the different microfocus X-ray diffraction patterns of Runs no. 20 and 11 in Figure 1. The SEM-EDS analysis showed that the new phase coexisting with corundum-type Cr_2O_3 has the atomic ratio Mg : Cr = 1.99(1) : 2.00(1), indicating $Mg_2Cr_2O_5$ composition (Table 2). The powder X-ray diffraction pattern of the new $Mg_2Cr_2O_5$ phase was very similar to that of mLd-type $Mg_2Al_2O_5$ (Enomoto et al., 2009). As described below, the structure refinement confirmed that the basic structure of the $Mg_2Cr_2O_5$ is the mLd structure.

At 16-18 GPa and 1100-1600°C, the two phases combine into a single $MgCr_2O_4$ phase whose Mg : Cr ratio was determined to be 1.01(1) : 1.99(1) by the SEM-EDS analysis. The microfocus X-ray diffraction pattern of the phase is shown as Run no. 3 in Figure 1. The microfocus and powder X-ray diffraction patterns of the $MgCr_2O_4$ phase resembled well that of $CaTi_2O_4$. As shown below, Rietveld refinement confirmed that the $MgCr_2O_4$ phase has the CT-type structure. The CT-type $MgCr_2O_4$ is stable at pressure up to at least 28 GPa. The cell parameters determined by Rietveld refinements of mLd-type $Mg_2Cr_2O_5$ and CT-type $MgCr_2O_4$ are summarized in Table 3. Using the cell parameters, densities of the mixture of mLd-type $Mg_2Cr_2O_5$ + Cr_2O_3 corundum (Belokoneva and Shcherbakova, 2003) and CT-type $MgCr_2O_4$ are calculated as 4.77(4) and 4.878(1) g/cm^3, respectively. Therefore, density increase from $MgCr_2O_4$ spinel (4.415(1) g/cm^3) (Lenaz et al., 2004) to the mixture of mLd-type $Mg_2Cr_2O_5$ + Cr_2O_3 corundum is 8.0%, and that from the mixture to CT-type $MgCr_2O_4$ is 2.3%.

The microfocus X-ray diffraction pattern in Figure 1 for Run no. 13 made at 15.9 GPa and 1000°C shows that the recovered sample contained MgO periclase and Cr_2O_3 corundum together with $MgCr_2O_4$ spinel, though that of Run no. 20 made at 13.5 GPa and 1200°C shows the single-phase spinel. This indicates that a part of $MgCr_2O_4$ spinel in Run no. 13 dissociated into the mixture of MgO periclase and Cr_2O_3 corundum. The presence of $MgCr_2O_4$ spinel in the run product no. 13 can be attributed to sluggish kinetics of the decomposition reaction at the relatively low temperature. Therefore, we interpreted that MgO periclase + Cr_2O_3 corundum are stable at 1000 °C at about 14-17 GPa. This assemblage changes into the mixture of mLd-type $Mg_2Cr_2O_5$ and Cr_2O_3 corundum at 17 GPa and 1000°C. At pressure above 20 GPa and temperature below 1000°C, the recovered samples showed weak, broad X-ray diffraction pattern different from all the phases

mentioned above, suggesting that another new phase may be stable at the P,T conditions and transform to the phase of the broad, weak X-ray pattern during decompression. A further study is necessary to clarify the possible stable phase in the P,T conditions. Fan et al. (2008) found that any phase transitions in the natural chromium spinel were not observed up to 26.8 GPa and 628 K. However, we made the high-pressure experiments at higher temperature than theirs. The density of the mixture of MgO periclase (Boiocchi et al. 2001) and Cr_2O_3 corundum, 4.78(4) g/cm^3, agrees within the errors with that of the mixture of mLd-type $Mg_2Cr_2O_5$ and Cr_2O_3 corundum at ambient conditions. However, the phase transition experiments indicate that the mixture of mLd-type $Mg_2Cr_2O_5$ and Cr_2O_3 corundum is stable at higher pressure than MgO periclase + Cr_2O_3 corundum, suggesting that the latter assemblage is slightly less dense than the former at high pressure and high temperature.

2. Crystal structures of $CaTi_2O_4$-type $MgCr_2O_4$ and modified ludwigite-type $Mg_2Cr_2O_5$.

We show the results of structure analyses of CT-type $MgCr_2O_4$ and mLd-type $Mg_2Cr_2O_5$ in Tables 2-4 and Figures 3-5. The crystal structures illustrated in Figures 3-5 were drawn by VESTA (Momma and Izumi, 2008). The structural parameters and reliability indexes (R_{wp}, R_e, R_B, and R_F) of CT-type $MgCr_2O_4$ and mLd-type $Mg_2Cr_2O_5$ are shown in Table 4. The R_{wp}, R_B and R_F values converged to sufficiently small values (<5%) indicate that results of the structure refinements are reliable for CT-type $MgCr_2O_4$ and mLd-type $Mg_2Cr_2O_5$. The interatomic distances, bond angles, effective coordination numbers (n_c) (Nespolo et al., 2001) and the bond valence sum (BVS) values (Brown and Altermatt, 1985) of CT-type $MgCr_2O_4$ and mLd-type $Mg_2Cr_2O_5$ are shown in Table 5. In the following section, we explain detailed results on structure analyses of

01 both the phases.

02

03 (a) $CaTi_2O_4$-type $MgCr_2O_4$

04 The results of Rietveld refinement of CT-type $MgCr_2O_4$ are given in Tables 3-4 and Figure 3a. In the
05 refinement, isotropic atomic displacement parameters of all of oxygen of CT-type $MgCr_2O_4$ were refined with
06 the common value. As shown in Figure 4, the coordination number of Mg in the tunnels surrounded by four
07 double chains of edge-shared octahedra is eight (bicapped trigonal prism). We compare structure parameters of
08 CT-type $MgCr_2O_4$ with those of $CaTi_2O_4$ (Bertaut and Blum, 1956) and CT-type $FeCr_2O_4$ (Ishii et al., in press).
09 The average Cr-O distance of the CrO_6 octahedron, 1.990 Å, is close to the sum of effective ionic radii of Cr^{3+}
10 (0.615 Å for six-fold coordination) and O^{2-} (1.40 Å for six-fold coordination) (Shannon, 1976). The bond
11 angles of O1-Cr1-O3 and O2-Cr1-O3 are 172.4° and 179.8°, respectively, which are in good agreement with
12 those by single-crystal structure analysis by Bindi et al. (2014). On the other hand, those of O1-Ti1-O3 and
13 O2-Ti1-O3 of $CaTi_2O_4$ are 171.2° and 166.2°, respectively. Therefore, CrO_6 octahedral site of CT-type
14 $MgCr_2O_4$ is closer to the regular octahedron than TiO_6 octahedral site of $CaTi_2O_4$. The difference of bond
15 angles of two corner-shared double chains between CT-type $MgCr_2O_4$ and $CaTi_2O_4$ is considerably large
16 (124.4° of Cr1-O2-Cr1 and 141.6° of Ti1-O2-Ti1). The bond angle difference is probably attributed to the large
17 difference in ion radii between Mg^{2+} and Ca^{2+} which occupy the tunnel sites. In fact, the Cr1-O2-Cr1 angle in
18 CT-type $FeCr_2O_4$ (Ishii et al., in press) is a similar value, 124.1°, to that in CT-type $MgCr_2O_4$. The Mg-O
19 distances in the MgO_8 bicapped trigonal prism are 1.99-2.27 Å for Mg-O distances in MgO_6 prism and 2.63 Å
20 for two longer Mg-O bonds. On the other hand, the Ca-O distances in the CaO_8 bicapped trigonal prism of

21 $CaTi_2O_4$ are 2.32-2.46 Å (CaO_6 prism) and 2.74 Å (two longer Ca-O bonds). The effective coordination
22 numbers (n_c) (Nespolo et al., 2001) of Mg^{2+} and Ca^{2+} were obtained to be 4.93 and 6.86, respectively. The
23 smaller n_c value of CT-type $MgCr_2O_4$ is caused by the two very long Mg-O bonds, compared with sum of
24 effective ion radii of Mg^{2+} (0.89 Å for eight-fold coordination) and O^{2-} (1.40 Å for six-fold coordination)
25 (Shannon, 1976). This implies that the coordination number of Mg^{2+} with oxygen in the tunnel spaces is 6
26 rather than 8. In CT-type $FeCr_2O_4$, the coordination number of Fe^{2+} is also regarded as 6 (Ishii et al., in press).
27
28 (b) Modified ludwigite-type $Mg_2Cr_2O_5$
29 Figure 3b shows the results of Rietveld refinement of $Mg_2Cr_2O_5$ phase. When we adopted mLd-type
30 $Mg_2Al_2O_5$ as the structure model, the reliability indexes sufficiently converged, as shown by the values of R_{wp}
31 (1.982%), R_B (3.294%) and R_F (4.337%) in Table 4. In the refinement, isotropic atomic displacement
32 parameters of all of oxygen of $Mg_2Cr_2O_5$ phase were refined with the common value. We found, however, that
33 very weak extra-diffraction peaks exist at the relatively low angle range (2θ = 3-10°) in Figure 3b. This may
34 suggest a possibility of superstructure, though the basic structure of $Mg_2Cr_2O_5$ phase is the mLd-type. The
35 study on the possible superstructure of $Mg_2Cr_2O_5$ phase by TEM observation is currently in progress. In this
36 paper, we assume that $Mg_2Cr_2O_5$ phase has the mLd-type structure. Figure 5 shows the crystal structure of the
37 mLd-type $Mg_2Cr_2O_5$, which has five non-equivalent cation sites (M1 – M5). The M1-M4 sites are octahedral
38 sites, while the M5 site forms a six-coordinated prism. Because Cr^{3+} has high octahedral-preference due to its
39 high crystal-field stabilization energy, we assume that all of Cr^{3+} ions are in M1-M4 sites. In the M1-M4 sites,
40 average cation-oxygen distances (2.005-2.088 Å) in each site are somewhat different from Mg-O and Cr-O

distances calculated from effective ionic radii of Mg^{2+} (0.72 Å for six-fold coordination), Cr^{3+} (0.615 Å for six-fold coordination) and O^{2-} (1.40 Å for six-fold coordination) (Shannon, 1976). Therefore, we determined the site occupancies of Mg^{2+} and Cr^{3+} in the M1-M4 sites from the average interatomic distances, and the results are shown in Table 5. The M5 site is placed in the zigzag framework of edge-shared octahedra, and in the M5 site Mg^{2+} is coordinated by six oxygens to form MgO_6 prism. The average Mg-O distance of MgO_6 prism is 2.141 Å, and is close to 2.12 Å, the sum of effective ionic radii of Mg^{2+} (0.72 Å) and O^{2-} (1.40 Å) (Shannon, 1976). These results reveal that the basic structure of the $Mg_2Cr_2O_5$ phase is correctly the mLd-type. The above features of the $Mg_2Cr_2O_5$ structure are similar to those of the mLd-type $Fe_2Cr_2O_5$ (Ishii et al., in press).

3. Implications to ultra-high pressure chromitites in the ophiolite.

Yang et al. (2007) found that the podiform chromitites in the Luobusa ophiolite contained high-pressure minerals such as diamonds and coesite. They interpreted that coesite was pseudomorphic mineral of stishovite which was originated from the deep upper-mantle (>9 GPa). Furthermore, Yamamoto et al. (2009) reported exsolution lamellae of coesite and clinopyroxene in chromite in the chromitites of the Luobusa ophiolite. Yamamoto et al. (2009) and Arai (2010, 2013) interpreted that these exsolution lamellae in chromite were formed by the processes associated with inverse transformation from CF-phase to chromite with exsolutions of coesite and clinopyroxene during mantle upwelling because CF-phase could dissolve CaO and SiO_2 components, and that ultrahigh-pressure chromitites in the Luobusa ophiolite were originated as CF-phase in the deep mantle at pressure above 12.5 GPa on the basis of the synthesis pressure of $FeCr_2O_4$-rich CF-phase

by Chen et al. (2003a, b). Our recent work (Ishii et al., in press) on precise determination of high-pressure phase relations in $FeCr_2O_4$ indicates that at 800-1600 °C $FeCr_2O_4$ chromite does not directly transform to CF-phase but first dissociates into the assemblage of mLd-type $Fe_2Cr_2O_5$ and Cr_2O_3 eskolaite at 12-16 GPa and subsequently transforms to CF- or CT-type $FeCr_2O_4$ at 16-18 GPa in the temperature range of 800-1600 °C. These transition behaviors in $FeCr_2O_4$ are very similar to those in $MgCr_2O_4$ of this study. Considering the results of both $FeCr_2O_4$ and $MgCr_2O_4$, it is very likely that the mixture of mLd-type $(Mg,Fe)_2Cr_2O_5$ + corundum-type Cr_2O_3 is stable in the pressure range of about 12-18 GPa in the $MgCr_2O_4$-$FeCr_2O_4$ system. The chemical composition of natural chromite in the chromitites reported by Yamamoto et al. (2009) is $(Mg_{0.77}, Fe^{2+}_{0.22})_{0.99}(Al_{0.42}, Cr_{1.46}, Fe^{3+}_{0.11})_{1.99}O_4$, which can be approximated as a solid solution in the $MgCr_2O_4$-$FeCr_2O_4$ system. Hence, we discuss on the above scenario that the natural chromite in the chromitites of the Luobusa ophiolite was originally CF- or CT-phase in the deep mantle and it converted to the spinel-structured chromite during mantle upwelling. In our high-pressure experiments, the completely dissociated two-phases, mLd-type $M_2Cr_2O_5$ + Cr_2O_3 corundum (M = Mg, Fe), whose grain sizes were about 3-5 μm were synthesized at about 13-18 GPa and 1400-1600 °C only for 1 h in both of $MgCr_2O_4$ and $FeCr_2O_4$ bulk compositions. Therefore, considering the mantle temperature around 1400-1600 °C appropriate at the depth range (Akaogi et al., 1989), it is likely that the CF- or CT-phase in the upwelling mantle could be completely decomposed into the two phases, mLd-type $(Mg,Fe)_2Cr_2O_5$ + corundum-type Cr_2O_3, of several mm or cm in size in the geological timescale. Once grain growth of the two phases has occurred, it would be rather difficult to completely react again to form the single-phase chromite with the spinel structure during the further upwelling process. It is noted that direct transition from CT- or CF-phase to chromite cannot occur in the upwelling process, on the basis of our phase

diagrams in $MgCr_2O_4$ (Figure 2) and $FeCr_2O_4$ (Figure 2 in Ishii et al., in press). In the studies of the natural chromitites in the Luobusa ophiolite, however, no evidences on presence of the decomposed phases, mLd-type $(Mg,Fe)_2Cr_2O_5$ + corundum-type Cr_2O_3, have been reported. Therefore, we would be able to put a constraint on the formation pressure for the Luobusa ophiolite chromitites: the chromitites have not undergone the mantle condition deeper than about 360-450 km corresponding to 12-15 GPa. Further studies are desirable to carefully examine whether the decomposed phases are present or not in the natural chromitites.

Acknowledgements

We thank T. Kunimoto and T. Irifune for useful discussions. We are grateful to the Associated Editor and reviewers for constructive comments and valuable suggestions. This research was partly supported by the Grants-in-Aid (nos. 22340163 and 25287145 to M. Akaogi, and 25289233 to K. Yamaura) of the Scientific Research of the Japan Society for the Promotion of Science (JSPS), by the Research Fellowship from JSPS for Young Scientists to T. Ishii, and by the Funding Program for World-Leading Innovative R&D on Science and Technology (FIRST Program), Japan. The synchrotron XRD measurements were made on the BL02B2 (proposal no. 2012A1658) and BL15XU (proposal nos. 2011B4514 and 2012A4512) of SPring-8 under the Priority Nanotechnology Support Program administered by the Japan Synchrotron Radiation Research Institute.

References cited

Akaogi, M., Ito, E., Navrotsky, A. (1989) The olivine-modified spinel-spinel transitions in the system Mg_2SiO_4-Fe_2SiO_4: calorimetric measurements, thermochemical calculation, and geophysical application,

Journal of Geophysical Research, 94, 15671-15685.

Arai, S. (2010) Possible recycled origin for ultrahigh-pressure chromitites in ophiolite. Journal of Mineralogical and Petrological Sciences, 105, 280-285, doi: 10.2465/jmps.100622a.

Arai, S. (2013) Conversion of low-pressure chromitites to ultrahigh-pressure chromitites by deep recycling: A good inference. Earth and Planetary Science Letters, 379, 81-87, doi.org/10.1016/j.epsl.2013.08.006.

Belokoneva, E.L., Shcherbakova, Y.K. (2003) Electron density in synthetic escolaite Cr_2O_3 with a corundum structure and its relation to antiferromagnetic properties, Russian journal of inorganic chemistry, 48, 861-869.

Boiocchi, M., Caucia, F., Merli, M., Prella, D., Ungaretti, L. (2001) Crystal-chemical reasons for the immiscibility of periclase and wüstite under lithospheric P, T conditions. European Journal of Mineralogy, 13, 871-881.

Bertaut, E.F. and Blum, P. (1956) Détermination de la Structure Ti_2CaO_4 par la Méthode Self-Consistence d'Approche Directe. Acta Crystallographica, 9, 121-125.

Bindi, L., Sirotkina, E., Bobrov, A.V., Irifune, T. (2014) X-ray single-crystal structural characterization of $MgCr_2O_4$, a post-spinel phase synthesized at 23 GPa and 1600 °C. Journal of Physics and Chemistry of Solids, 75, 638-641.

Brown, I.D., Altermatt, D. (1985) Bond-valence parameters obtained from a systematic analysis of the Inorganic Crystal Structure Database. Acta Crystallographica, B41, 244–247.

Chen, M., Shu, J., Xie, X., Mao, H.K. (2003a) Natural $CaTi_2O_4$-structure $FeCr_2O_4$ polymorph in the Suizhou meteorite and its significance in mantle mineralogy. Geochimica et Cosmochimica Acta, 67, 3937-3942, doi:

10.1016/S0016-7037(03)00175-3.

Chen, M., Shu, J., Mao, H.K., Xie, X., Hemley, R.J. (2003b) Natural occurrence and synthesis of two new postspinel polymorphs of chromite. Proc. Natl. Acad. Sci. USA, 100, 14651-14654, doi/10.1073/pnas.2136599100.

Dobrzhinetskaya, L., Wirth, R., Yang, J.-S., Hutcheon, I., Weber, P., Green, H.W., 2009. High pressure highly reduced nitride sand oxides from chromite of a Tibetan ophiolite. Proc. Natl. Acad. Sci. USA 106, 19233–19238.

Dunn, K.J., Bundy, F.P., (1978) Materials and techniques for pressure calibration by resistance-jump transitions up to 500 kilobars. Review of Scientific Instruments, 49, 365-370.

Enomoto, A., Kojitani, H., Akaogi, M., Yusa, H. (2009) High-pressure transitons in $MgAl_2O_4$ and a new high-pressure phase of $Mg_2Al_2O_5$. Journal of Solid State Chemistry, 182, 389-395, doi:10.1016/j.jssc.2008.11.015.

Fan, D., Zhou, W., Liu, C., Liu, Y., Jiang, X., Wan, F., Liu, J., Li, X., Xie, H., 2008. Thermal equation of state of natural chromium spinel up to 26.8 GPa and 628 K. Journal of Material Science, 43, 5546–5550.

Fei, Y., Orman, J. Van., Li, J., Western, W. Van., Sanloup, C., Minarik, W., Hirose, K., Komabayashi, T. (2004). Experimentally determined post-spinel transformation boundary Mg_2SiO_4 using MgO as an internal pressure standard and its geophysical implications. Journal of Geophysical Research, 109, doi: 10.1029/2003JB002562.

Irifune, T., Naka, H., Sanehira, T., Inoue T., Funakoshi, K., (2002) In situ X-ray observations of phase transitions in $MgAl_2O_4$ spinel to 40 GPa using multianvil apparatus with sintered diamond anvils. Physics

and Chemistry of Minerals, 29, 645-654.

Ishii, T., Kojitani, H., Akaogi, M., (2011) Post-spinel transitions in pyrolite and Mg_2SiO_4 and akimotoite-perovskite transition in $MgSiO_3$: Precise comparison by high-pressure high-temperature experiments with multi-sample cell technique. Earth and Planetary Science Letters, 309, 185-197, doi: 10.1016/j.epsl.2011.06.023.

Ishii, T., Kojitani, H., Akaogi, M., (2012) High-pressure phase transitions and subduction behavior of continental crust a pressure-temperature conditions up to the upper part of the lower mantle. Earth and Planetary Science Letters, 357-358, 31-41, doi: 10.1016/j.epsl.2012.09.019.

Ishii, T., Kojitani, H., Tsukamoto, S., Fujino, K., Mori, D., Inaguma, Y., Tsujino, N., Yoshino, T., Yamazaki, D., Higo, Y., Funakoshi, K., Akaogi, M. (2014) High-pressure phase transitions in $FeCr_2O_4$ and structure analysis of new post-spinel $FeCr_2O_4$ and $Fe_2Cr_2O_5$ phases with meteoritical and petrological implications. American Mineralogist, in press, DOI: 10.2138/am.2014.4736.

Ishii, T., Mori, D., Inaguma, Y., Fujino, K., Matsushita, Y., Yamaura, K., Kojitani, H., Akaogi, M. (2013) High-pressure phase relations in $FeCr_2O_4$ and $MgCr_2O_4$ and crystal structures of new post-spinel phases. Abstract of the 3rd Global-COE International Symposium on Deep Earth Mineralogy, p.44-45, March 2013, Matsuyama.

Ito, E. (2007) Theory and Practice – Multianvil cells and high-pressure experimental methods, in: G. Schubert, B. Romanowicz, A. Dziewonski (Eds.), Mineral Physics, 2, pp. 197-230. Treatise on Geophysics, Elsevier, Amsterdam.

Izumi, F., and Momma, K. (2007) Three-dimensional visualization in powder diffraction. Solid State

Phenomena, 130, 15-20.

Kojitani, H., Enomoto, A., Tsukamoto, S., Akaogi, M., Miura, H., Yusa, H. (2010) High-pressure high-temperature phase relations in $MgAl_2O_4$. Journal of physics: Conference Series, 215, 012098, doi:10.1088/1742-6596/215/1/012098.

Lenaz, D., Skogby, H., Princivalle, F., Halenius, U. (2004) Structural changes and valence states in the $MgCr_2O_4$-$FeCr_2O_4$ solid solution series. Physics and Chemistry of Minerals, 31, 633-642, doi: 10.1007/s00269-004-0420-0.

Louër, D. and Boultif, A. (2007) Powder pattern indexing and the dichotomy algorithm. Zeitschrift für Kristallographie Supplements, 26, 191-196, doi: 10.1524/zksu.2007.2007.suppl_26.191.

Momma, K. and Izumi, F. (2008) VESTA: a three-dimensional visualization system for electronic and structural analysis. Journal of Applied Crystallography, 41, 653-658.

Morishima, H., Kato, T., Suto, M., Ohtani, E., Urakawa, U., Shimomura, O., Kikegawa, T. (1994) The phase boundary between alpha-Mg_2SiO_4 and beta-Mg_2SiO_4 determined by in-situ x-Ray observation. Science, 265, 1202-1203.

Nespolo, M., Ferraris, G., Hoppe, R. (2001) Charge distribution analysis of ceramic materials. Journal of Ceramic Processing Research, 2, 38-44.

O'Neill, H.St.C., Dollase, W.A. (1994) Crystal structures and cation distributions in simple spinels from powder XRD structural refinements: $MgCr_2O_4$, $ZnCr_2O_4$, Fe_3O_4, and the temperature dependence of the cation distribution in $ZnAl_2O_4$. Physics and Chemistry of Minerals, 20, 541-555.

Sack, R.O, Ghiorso, M.S. (1991) Chromite as a petrogenetic indicator. Reviews in Mineralogy, 25, 323-353.

Shannon, R.D. (1976) Revised effective ionic radii and systematic studies of interatomic distances in halides and chalcogenides. Acta Crystallographica, A32, 751-767.

Suzuki, A., Ohtani, E., Morishima, H., Kubo, T., Kanbe, Y., Kondo, T. (2000). In situ determination of the phase boundary between wadsleyite and ringwoodite in Mg_2SiO_4, Geophysical Research Letters, 27, 803-806.

Yamamoto, S., Kojima, T., Hirose, K., Maruyama, S. (2009) Coesite and clinopyroxene exsolution lamella in chromites: *In-situ* ultrahigh-pressure evidence from podiform chromitites in the Luobusa ophiolite, southern Tibet. Lithos, 109, 314-322.

Yang, J.S., Dobrzhinetskaya, L., Bai, W.J., Fang, Q.S., Robinson, P.T., Zhang, J., Green, H.W. (2007) Diamond- and coesite-bearing chromitites from the Luobusa ophiolite, Tibet. Geology, 35, 875-878, doi: 10.1130/G23766A.

Yong, W., Botis, S., Shieh, S.R., Shi, W., Withers, A.C., (2012) Pressure-induced phase transition study of magnesiochromite ($MgCr_2O_4$) by Raman spectroscopy and X-ray diffraction. Physics of the Earth and Planetary Interiors, 196-197, 75-82.

Figure captions

Figure 1. Microfocus X-ray diffraction patterns at atmospheric pressure and room temperature for the starting material and recovered samples, Run no. 20 (13.5 GPa, 1200°C), no. 13 (15.9 GPa, 1000°C), no. 11 (17.6 GPa, 1200°C) and no. 3 (19.8 GPa, 1200°C). Pressure and temperature in parentheses indicate the conditions of high-pressure experiments. Sp, spinel-type $MgCr_2O_4$; mLd, modified ludwigite-type $Mg_2Cr_2O_5$; Es,

01 corundum-type Cr_2O_3 eskolaite; CT, $CaTi_2O_4$-type $MgCr_2O_4$; Pc, rocksalt-type MgO periclase, Re: Re capsule.

02

03 **Figure 2**. Phase diagram of $MgCr_2O_4$ at high pressure and high temperature. Solid circle, Sp; solid square, mLd
04 + Es; half closed diamond, mLd + Es + CT; solid diamond, CT; solid inverse triangle, Sp + Pc + Es. Solid lines
05 represent phase boundaries. A dashed line represents the extrapolated transition boundary of mLd + Es to CT.
06 Sp, spinel-type $MgCr_2O_4$; mLd, modified ludwigite-type $Mg_2Cr_2O_5$; Es, corundum-type Cr_2O_3 eskolaite; CT,
07 $CaTi_2O_4$-type $MgCr_2O_4$; Pc, rocksalt-type MgO periclase.

08

09 **Figure 3**. Rietveld refinements of $CaTi_2O_4$-type $MgCr_2O_4$ (a) and modified ludwigite-type $Mg_2Cr_2O_5$ (b). These
10 X-ray diffraction patterns were measured at atmospheric pressure and room temperature. Data points and solid
11 lines show the observed and the calculated profiles, respectively, and the residual curves between them are
12 shown at the bottom. Bragg peak positions are indicated by small ticks. The upper and lower ticks in Figure
13 3(a) are for CT-type $MgCr_2O_4$ and corundum-type Cr_2O_3 (eskolaite), respectively. The ticks in Figure 3(b) are
14 for mLd-type $Mg_2Cr_2O_5$. The refined crystal structure is shown in each profile.

15

16 **Figure 4**. (a) and (b) Crystal structure of $CaTi_2O_4$-type $MgCr_2O_4$ in b-c and a-c planes, respectively. (c)
17 Coordination environments of Mg and Cr. (d) Mg-O distances and coordination environment of Mg.

18

19 **Figure 5**. (a) and (b) Crystal structure of modified ludwigite-type $Mg_2Cr_2O_5$ in a-b and b-c planes, respectively.
20 (c) Coordination environments for Mg and Cr in M1-M5 sites. Occupancies of Mg and Cr in each site of

M1-M4 are shown with the areas in each circle. (d) Mg-O distances and coordination environment of Mg in M5 site.

Table 1

Results of high-pressure high-temperature experiments

Run no.	Pressure (GPa)	Temperature (°C)	Time (min)	[a]Phases
34	13.9	1000	60	Sp
7	14.7	1000	120	Sp+Pc+Es
13	15.9	1000	120	Sp+Pc+Es
15	16.6	1000	120	Sp+Pc+Es
23	17.6	1000	120	mLd+Es
33	15.1	1100	60	mLd+Es
31	15.9	1100	120	mLd+Es

41	10	19.8	1100	60	CT
42	30	28.0	1100	120	CT
43	20	13.5	1200	60	Sp
44	19	14.7	1200	60	mLd+Es
45	11	17.6	1200	60	mLd+Es
46	22	18.6	1200	60	CT+mLd(tr)+Es
47	3	19.8	1200	60	CT
48	18	22.8	1200	60	CT
49	24	25.0	1200	60	CT
50	25	22.8	1300	60	CT
51	27	27.0	1300	60	CT
52	28	28.0	1300	60	CT
53	14	13.0	1400	60	Sp
54	5	13.9	1400	60	mLd+Es
55	16	14.7	1400	60	mLd+Es
56	17	17.6	1400	60	CT+mLd+Es
57	21	18.6	1400	60	CT
58	26	19.8	1400	60	CT
59	1	19.8	1500	60	CT
60	12	11.7	1600	60	Sp

61	8	13.0	1600	60	mLd+Es
62	4	14.7	1600	60	mLd+Es
63	9	15.9	1600	60	mLd+Es
64	6	16.6	1600	60	CT+mLd(tr)+Es
65	2	23.0	1600	60	CT

66 [a]Phases in the recovered samples.

67 Abbreviations: Sp, spinel-type $MgCr_2O_4$; mLd, modified ludwigite-type $Mg_2Cr_2O_5$; Es, corundum-type Cr_2O_3

68 (escolaite) ; Pc, MgO periclase; CT, $CaTi_2O_4$-type $MgCr_2O_4$; tr, trace.

69

70 Table 2

71 Chemical compositions of Spinel(Sp)-type $MgCr_2O_4$, $CaTi_2O_4$ (CT)-type $MgCr_2O_4$ and modified ludwigite

72 (mLd)-type $Mg_2Cr_2O_5$.

73		[a]Sp-type $MgCr_2O_4$	[b]CT-type $MgCr_2O_4$	[b]mLd-type $Mg_2Cr_2O_5$
74	MgO	20.85(28)	21.39(9)	34.75(21)
75	Cr_2O_3	78.35(44)	78.83(78)	65.78(40)
76	Total	99.20	100.22	100.52
77				
78	O	4	4	5
79	Mg	1.00(1)	1.01(1)	1.99(1)
80	Cr	2.00(1)	1.99(1)	2.00(1)

C.T.	3.00(1)	3.01(1)	4.00(1)

[a]Starting material

[b]Samples used for synchrotron XRD measurements

Abbreviations: C.T., cation total

Table 3

Lattice parameters of $CaTi_2O_4$ (CT)-type $MgCr_2O_4$ and modified ludwigite (mLd)-type $Mg_2Cr_2O_5$.

Phase	CT-type $MgCr_2O_4$	mLd-type $Mg_2Cr_2O_5$
Space group	*Cmcm* (no. 63)	*Pbam* (no. 55)
a (Å)	2.85107(2)	9.62894(7)
b (Å)	9.48930(8)	12.4625(1)
c (Å)	9.67853(8)	2.85644(2)
V (Å^3)	261.849(4)	342.775(5)
Z	4	4
V_m (cm^3/mol)	39.421(1)	51.605(1)
D (g/cm^3)	4.878(1)	4.507(1)

Table 4

Structure parameters of $CaTi_2O_4$ (CT)-type $MgCr_2O_4$ and modified ludwigite (mLd)-type $Mg_2Cr_2O_5$.

Atom	Wyckoff site	*g* (Mg)	*g* (Cr)	*x*	*y*	*z*	U_{iso} (Å^2)
CT-type $MgCr_2O_4$							
Mg	4*c*	1.0	0.0	0	0.1090(2)	0.25	0.0148(4)
Cr	8*f*	0.0	1.0	0	0.3670(1)	0.0707(1)	0.0076(1)
O1	4*b*	-	-	0	0	0	0.0033(2)
O2	4*c*	-	-	0	0.4629(3)	0.25	0.0033(2)
O3	8*f*	-	-	0	0.2676(2)	0.6134(1)	0.0033(2)
mLd-type $Mg_2Cr_2O_5$							
M1	2*a*	0.3	0.7	0	0	0	0.0067(3)

21	M2	2*d*	0.9	0.1	0	0.5	0.5	0.0140(5)
22	M3	4*g*	0.2	0.8	0.0202(1)	0.2883(1)	0	0.0110(2)
23	M4	4*h*	0.2	0.8	0.2717(1)	0.3843(1)	0.5	0.0072(2)
24	M5	4*g*	1.0	0.0	0.2431(1)	0.1310(1)	0	0.0169(4)
25	O1	4*h*	-	-	0.1413(2)	0.0310(2)	0.5	0.0067(2)
26	O2	4*g*	-	-	0.4049(2)	0.3514(2)	0	0.0050(2)
27	O3	4*h*	-	-	0.4019(5)	0.1440(2)	0.5	0.0050(2)
28	O4	4*g*	-	-	0.1335(3)	0.4287(2)	0	0.0050(2)
29	O5	4*h*	-	-	0.1578(3)	0.2468(2)	0.5	0.0050(2)

30 The reliability indexes for the CT-type $MgCr_2O_4$.

31 R_{wp} = 2.218%, R_e = 0.170%

32 CT-type $MgCr_2O_4$: R_B = 2.777%, R_F = 1.598%

33 Corundum-type Cr_2O_3: R_B = 5.980%, R_F = 2.932%

34 The reliability indexes for the mLd-type $Mg_2Cr_2O_5$.

35 R_{wp} = 1.982%, R_e = 0.163%

36 mLd-type $Mg_2Cr_2O_5$: R_B = 3.294%, R_F = 4.337%

37 $$R_{wp} = \left\{\frac{\sum_i w_i[y_i - f_i(x)]^2}{\sum_i w_i y_i^2}\right\}^{1/2},\ R_B = \frac{\sum_K |I_0(h_K) - I(h_K)|}{\sum_K I_0(h_K)},\ R_F = \frac{\sum_K ||F_0(h_K)| - |F(h_K)||}{\sum_K |F_0(h_K)|},\ R_e = \left\{\frac{N-P}{\sum_i w_i y_i^2}\right\}^{1/2}$$

38 where y_i, w_i and $f_i(x)$ are the intensity observed at step i, the statistical weight and theory intensity, respectively.

39 $I_0(\boldsymbol{h}_K)$, $I(\boldsymbol{h}_K)$, $F_0(\boldsymbol{h}_K)$ and $F(\boldsymbol{h}_K)$ are the observed and calculated intensities and structure factors for reflection K,

40 respectively. N and P are number of all data points and refined parameters, respectively.

41 g(M): site occupancy of M.

42

43

44

45

46

47

48

49

50 Table 5

51 Interatomic distances and angles in the structures of $CaTi_2O_4$ (CT)-type $MgCr_2O_4$ and modified ludwigite

52 (mLd)-type $Mg_2Cr_2O_5$.

53 CT-type $MgCr_2O_4$

54 Bond length (Å)				Bond angles (°)	
55 Mg–O2^{i} × 2	1.989(2)	Cr–O3^{iii} × 2	1.958(1)	O1^{vi} –Cr1– O3^{iii}	172.4(1)
56 Mg–O3^{ii} × 4	2.270(1)	Cr–O2	1.960(1)	O2–Cr1–O3^{iv}	179.8(1)
57 Mg–O1 × 2	2.631(1)	Cr–O3^{iv}	2.016(2)	Cr1^{vii}–O1–Cr1^{viii}	89.58(4)
58 Average	2.290	Cr–O1^{v} × 2	2.023(1)	Cr1^{vii}–O1^{vi}–C^{vi}	90.42(4)
59 n_c	4.93	Average	1.990	Cr1–O2–Cr1^{iv}	124.7(1)
60 BVS	1.90	n_c	5.95	Cr1^{ix}–O3–Cr1^{x}	93.44(10)

61			BVS	2.94	$Cr1^{ix}$–O3–$Cr1^{iv}$	96.81(9)
62						
63	mLd-type $Mg_2Cr_2O_5$					
64	Bond length (Å)					
65	M1 site		M2 site		M3 site	
66	M1–O1 × 4	2.010(2)	$M2–O3^{x}$ × 2	2.028(3)	$M3–O2^{x}$ × 2	2.012(2)
67	$M1–O2^{x}$ × 2	2.066(3)	M2–O4 × 4	2.117(2)	M3–O3 × 2	2.016(2)
68	Average	2.029	Average	2.088	M3–O4	2.062(3)
69	n_c	5.97	n_c	5.91	$M3–O5^{x}$	2.064(3)
70	BVS	2.43	BVS	2.07	Average	2.030
71					n_c	5.97
72					BVS	2.42
73	M4 site		M5 site			
74	M4–O1 × 2	1.963(2)	M5–O1 × 2	2.099(2)		
75	$M4–O2^{xi}$	2.011(3)	M5–O3 × 2	2.134(3)		
76	M4–O4 × 2	2.029(2)	M5–O5 × 2	2.190(3)		
77	M4–O5	2.035(3)	Average	2.141		
78	Average	2.005	n_c	5.93		
79	n_c	5.95	BVS	1.80		
80	BVS	2.59				

Bond angles (°)

O1–M1–O1^{vii}	90.6(1)	M3^{ix}–O2vi–M1^{xii}	121.2(2)	M3^{ix}–O3–M3^{xv}	90.5 (1)
O1–M1–O2^{x}	97.32(7)	M1–O1–M1^{xii}	90.6(1)	M3–O5–M3^{xii}	90.2(2)
O4–M2–O4^{xii}	84.85(8)	M4–O2–M1^{xiii}	95.85(3)	M4^{vii}–O4–M3	96.64(5)
O3^{x}–M2–O4^{xii}	84.92(8)	M1^{xii}–O1–M4^{xiv}	96.15(5)	M3^{xii}–O5–M4	97.95(5)
O3^{x}–M3–O5^{vii}	169.29(9)	M2–O4–M2^{vii}	84.9(1)	M4^{vii}–O2–M3^{ix}	121.85(4)
O4–M3–O2^{x}	179.4(2)	M3–O4–M2^{vii}	92.0(1)	M4–O2–M4^{vii}	93.4(1)
O2–M4–O4^{xii}	176.12(1)	M3^{xv}–O3–M2^{ix}	96.2(1)	M4–O4–M4^{vii}	89.5(1)
O1^{xi}–M4–O5	172.0(2)	M4^{vii}–O4–M2^{vii}	92.16(3)		

Symmetry codes: (i) 1/2+x, y−1/2, z. (ii) −1/2−x, 1/2−y, 1−z. (iii) 1/2−x, 1/2−y, z−1/2. (iv) x, y, 1/2−z. (v) 1/2+x, 1/2+y, z. (vi) x−1/2, 1/2+y, z. (vii) 1/2−x, 1/2−y, −z. (viii) −x−1/2, 1/2−y, −z. (ix) 1/2−x, 1/2−y, 1/2+z. (x) −x−1/2, 1/2−y, 1/2+z. (xi) 1/2+x, 1/2+y, 1/2−z. (xii) x, y, z+1. (xiii) −x, −y, 1/2+z. (xiv) 1/2+x, y−1/2, 1/2−z. (xv) 1/2−x, 1/2−y, 3/2+z.

n_c: effective coordination number

BVS: bond valence sum value

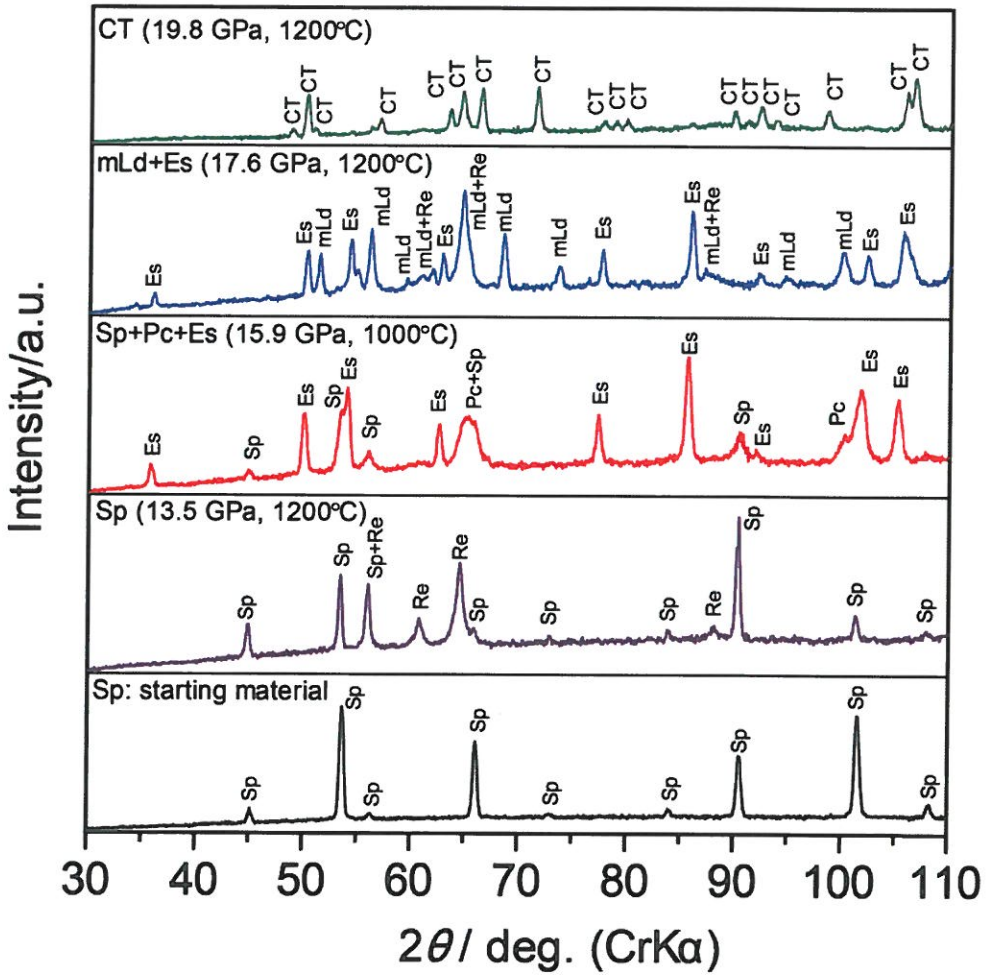
CT (19.8 GPa, 1200°C)
mLd+Es (17.6 GPa, 1200°C)
Sp+Pc+Es (15.9 GPa, 1000°C)
Sp (13.5 GPa, 1200°C)
Sp: starting material
Intensity/a.u.
30 40 50 60 70 80 90 100 110
2θ/ deg. (CrKα)

Figure 1.

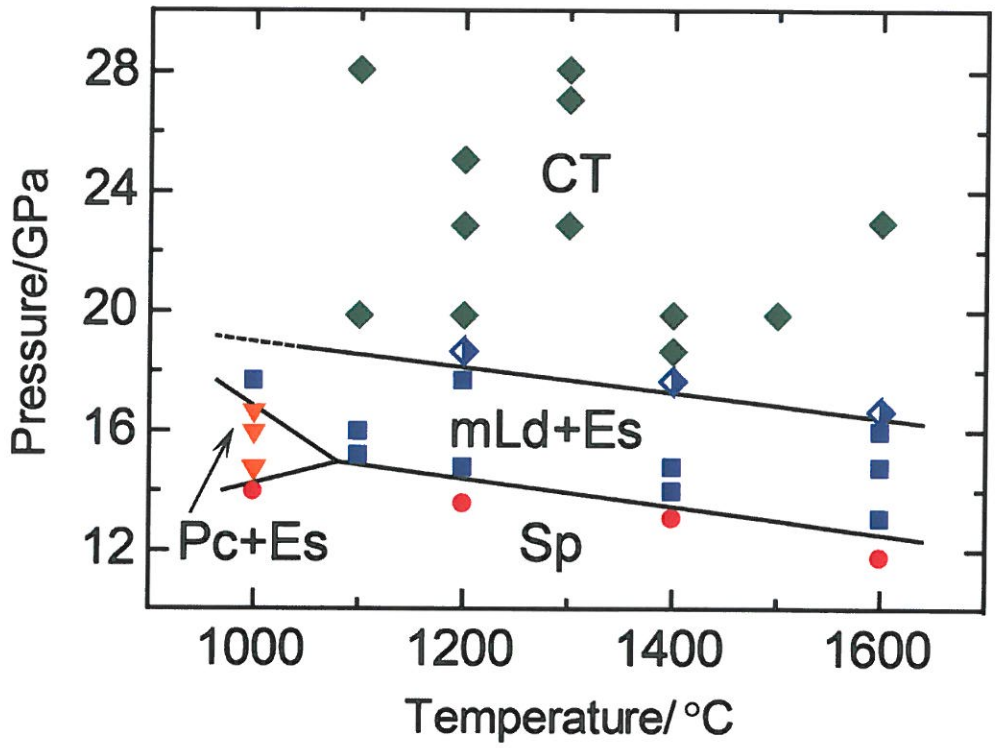
28
24
20
16
12
Pressure/GPa
CT
mLd+Es
Pc+Es
Sp
1000
1200
1400
1600
Temperature/ °C

Figure 2

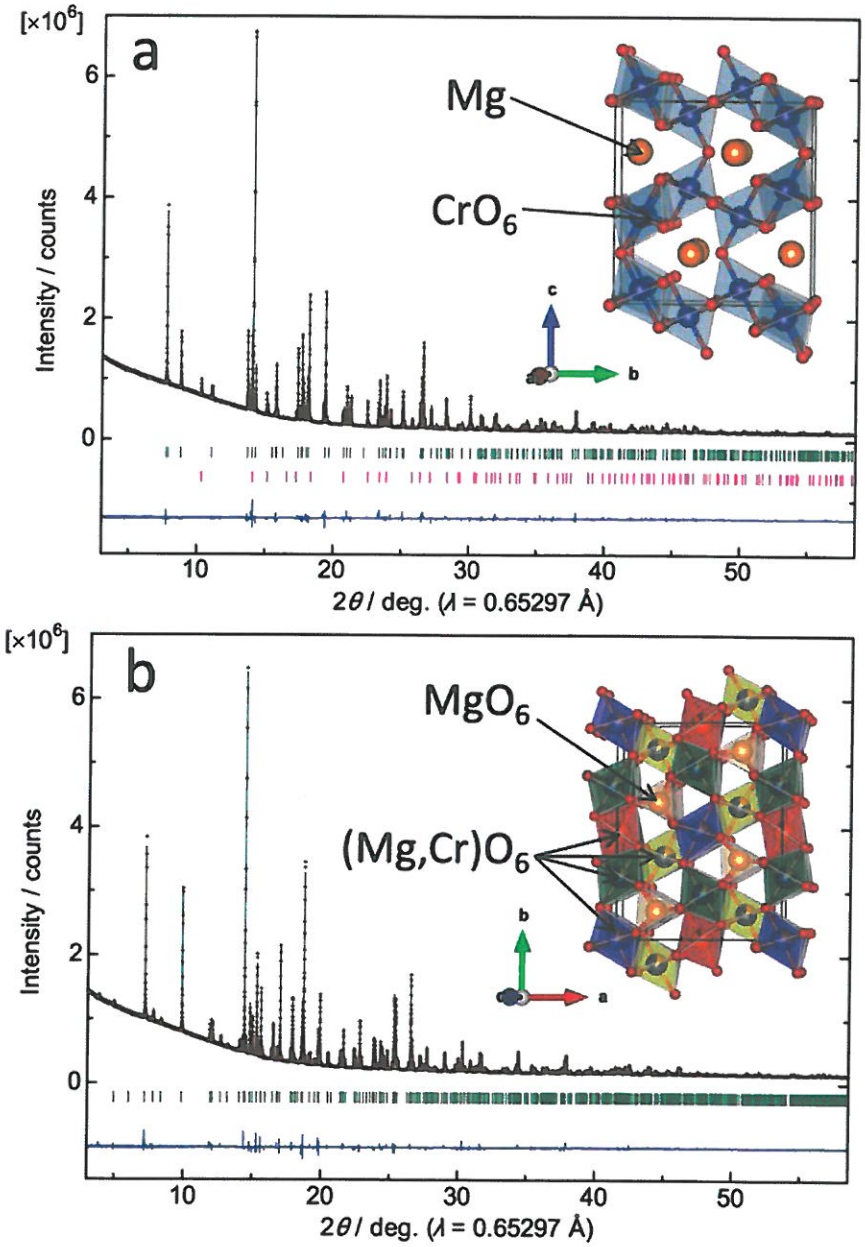
[×10^6]
a
Mg
CrO6
c
b
Intensity / counts
2θ / deg. (λ = 0.65297 Å)
[×10^6]
b
MgO6
(Mg,Cr)O6
b
a
Intensity / counts
2θ / deg. (λ = 0.65297 Å)

Figure 3

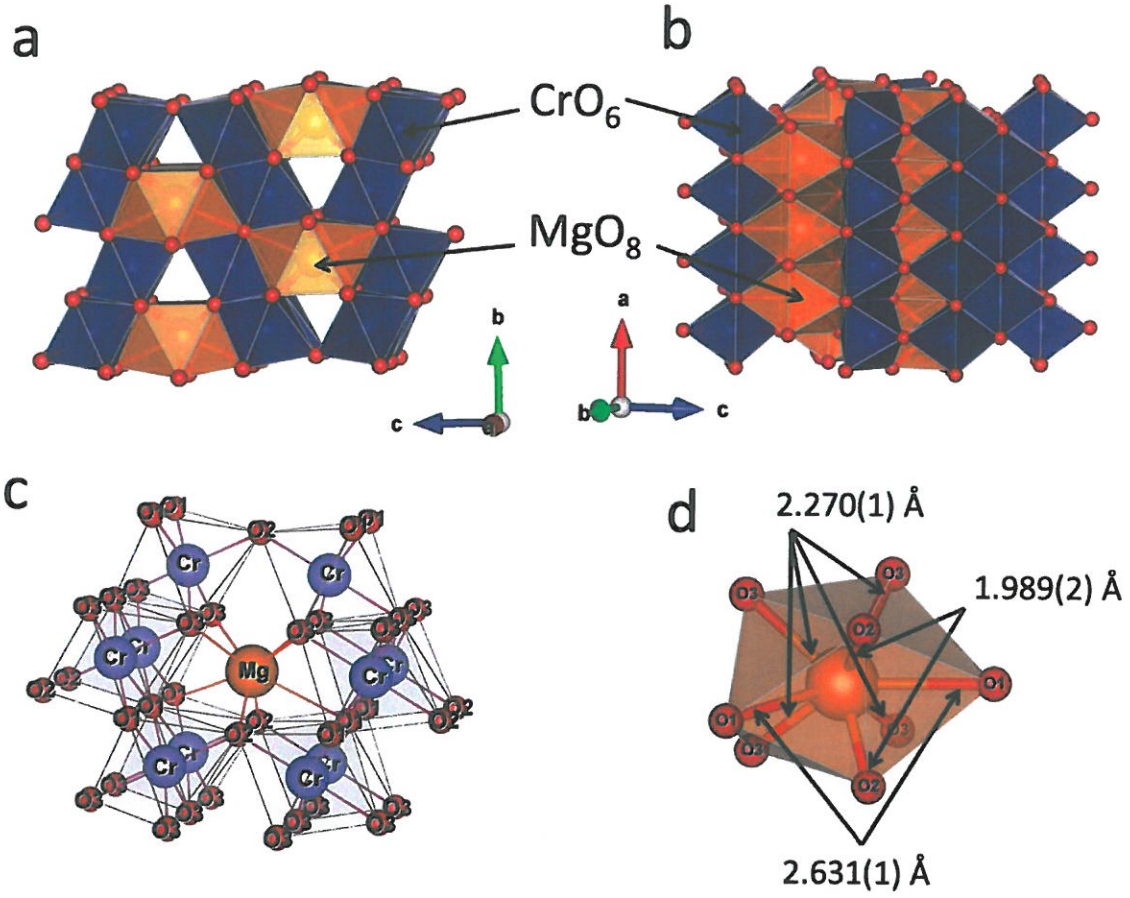

Figure 4

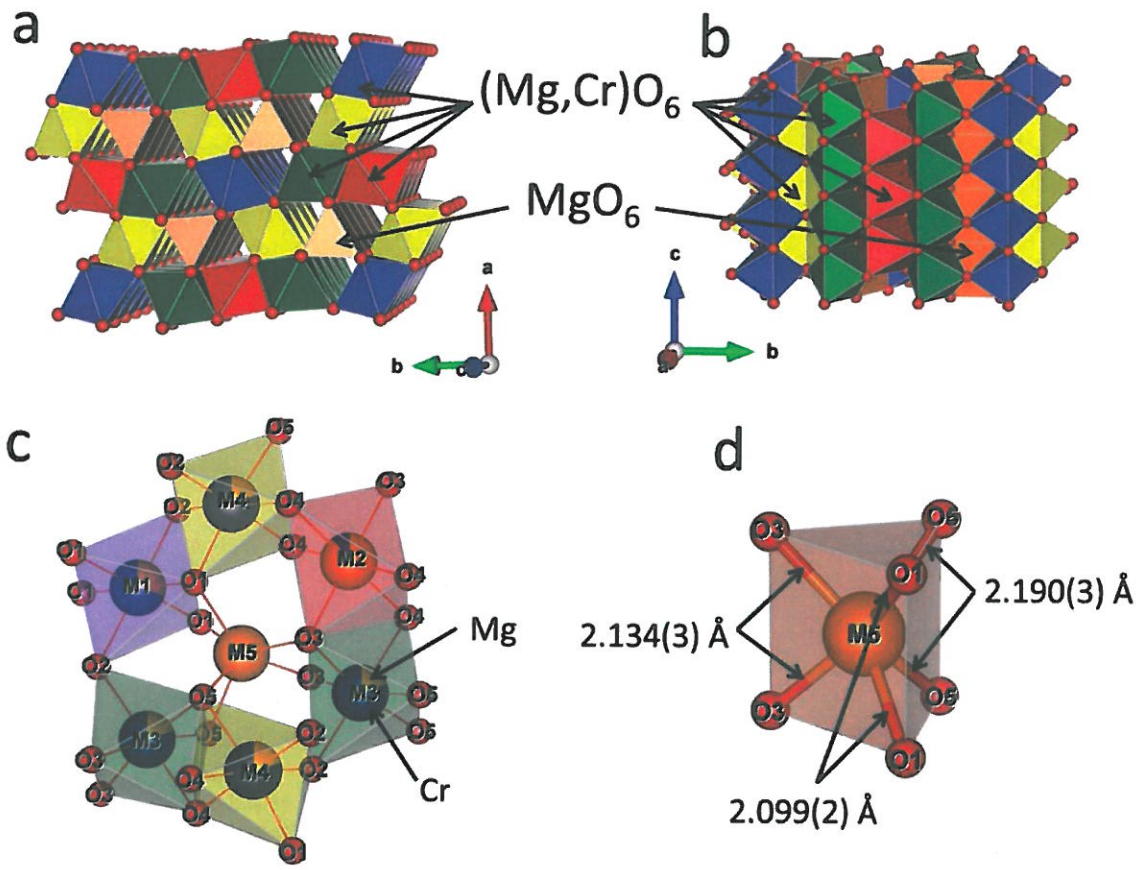

Figure 5